An Adaptive Spectrogram Estimator to Enhance Signal Characterization

Christian C. Jones[1], Zeus E. Gannon[1], Shannon D. Blunt[1], Christopher T. Allen[1], Anthony F. Martone[2]

[1]Radar Systems Lab (RSL), University of Kansas (KU), Lawrence, KS
[2]U.S. Army Research Laboratory (ARL), Adelphi, MD

Abstract—**Time-frequency (TF) analysis is employed in numerous applications to characterize the attributes of signals. For cognitive radar it can provide valuable information regarding the particular signals/systems encountered to support automated decision-making. Here an adaptive approach to spectrogram estimation is considered that relies on reiterative minimum mean-square error (RMMSE) estimation. Moreover, it is experimentally shown using open-air data that the combination of adaptive direction-finding (DF) and adaptive TF analysis provides enhanced signal characterization for congested spectral environments.**

Keywords—*adaptive processing, spectrogram, signal estimation, signal isolation*

I. INTRODUCTION

Today's complicated radio frequency (RF) environment is increasingly congested and dynamic [1, 2], with the latter an emerging response to the former. The arise of cognitive systems necessitates real-time determination of spectral occupancy (e.g. via [3]), with rapid characterization of observed signals also important for automated decision-making. A key challenge with cognitive systems is their focus on a single optimization task to improve performance, often pertaining to a particular time, frequency, spatial, or waveform dimension. For example, time-frequency dynamic spectrum access (DSA) cognitive radar approaches have been shown to be effective for coexistence with non-cooperative, ambient RF emitters [4]; however, DSA by itself cannot isolate spatial information (e.g. DF) and is limited to a particular application space. New methods are needed that exploit multidimensional aspects of spectral information and are practical to implement on realistic timescales (i.e. low latency).

In the cognitive sensing context, TF analysis encompasses a broad class of tools with which the time-varying spectral behavior of signals can be evaluated [5, 6], including linear approaches such as the short-time Fourier transform (STFT) and nonlinear approaches like the Wigner-Ville distribution [7]. Of these, the STFT is a widely used benchmark that offers a multi-resolution TF trade-space, with the resulting spectrogram providing a visualization of instantaneous frequency content that is commonly employed in a variety of applications spanning ecology, micro-Doppler, phonetics, musicology, neuroscience, astronomy, and more [4, 8, 9]. The spectrogram can also serve as preprocessing to aid machine learning [10].

Of course, the frequency resolution of the STFT is dictated by the temporal extent of the processing window, thereby often necessitating multi-resolution or wavelet analysis to achieve sufficient separability of TF components. Due to the inherent nonstationarity of signal structures – indeed, that is the very behavior being sought to understand – classical adaptive methods based on the formation of a sample covariance matrix of time snapshots (e.g. [11, 12]) are not always applicable.

Alternatively, reiterative minimum mean-square error (RMMSE) estimation, originally developed for adaptive pulse compression [13], is here repurposed to obtain a structure-based adaptive spectrogram that refines the TF estimate. The parallels between frequency and spatial estimation enables direct use of the RMMSE DF formulation denoted as reiterative super-resolution (RISR) [14] as well as its subsequent developments to enhance robustness [15, 16]. The key attributes of RISR that facilitate adaptive TF estimation are its ability to operate with extremely low sample support (even just a single snapshot), the incorporation of a tolerance term for model mismatch, and use of a tunable "partial constraint", the combination of which provide robustness to time-varying signals.

In the companion paper [17] these attributes were employed in conjunction with a self-calibration routine to experimentally demonstrate RISR in the context of DF for practical spatial isolation of co-channel signals occupying the same spectrum. Here, this process is reformulated for the TF application, and then experimentally demonstrated to enhance separability and visibility of TF components. Consequently, the sequential combination of these adaptive processes is shown to provide a practical way to achieve accurate TF analysis for increasingly congested spectral environments.

II. SPECTROGRAM SIGNAL MODEL

Consider the continuous-time receive capture

$$y(t) = s(t) + v(t) \qquad (1)$$

where $s(t)$ is some time-varying unknown signal and $v(t)$ is additive noise. Because (1) is captured over some finite time interval, $s(t)$ cannot be bandlimited, which means that aliasing in receive sampling is unavoidable (though possibly negligible). If we assume the use of some form of frequency-selective processing (e.g. [3]) to identify bands of interest and the absence (for now) of other spectrally overlapping signals, then this isolated signal-plus-noise perspective is meaningful. With that said, since the unknown signal $s(t)$ in (1) is arbitrary, it could also represent the combination

$$s(t) = \sum_{k=1}^{K} s_k(t) \qquad (2)$$

where multiple unknown signals are present, which will increasingly be the case given growing spectral congestion. Consequently, TF analysis in the context of (2) produces an aggregate response, which would necessitate some other means

of discrimination to separate the components. The companion paper [17] demonstrated the use of adaptive spatial isolation to realize this separation. In the experimental results later in this paper, both aggregated and spatially isolated versions of measured open-air data are examined.

Discretizing (1) at a rate that preserves noise-limited spectral content (i.e. passband and roll-off) yields the length-Q vector

$$\mathbf{y} = [y_0 \quad y_1 \quad \cdots \quad y_{Q-1}]^T, \tag{3}$$

where the STFT could be applied to different segments of varying extent to realize a multi-resolution TF response. Here we denote N as some minimum reasonable number of time samples (based on expected signal nonstationarity, nominal resolution, or other factors). Then (3) is decomposed into length-N overlapping segments denoted as

$$\bar{\mathbf{y}}(\ell) = [y_\ell \quad y_{\ell+1} \quad \cdots \quad y_{\ell+N}]^T, \tag{4}$$

according to discrete time index ℓ. For this time granularity and $\forall \ell$, the STFT can be performed to obtain the length-M

$$\hat{\mathbf{s}}_\text{f}(\ell) = \mathbf{A}^H \bar{\mathbf{y}}(\ell), \tag{5}$$

with $\mathbf{A}^H$ the discrete Fourier transform, subscript 'f' signifying the frequency domain, and the "hat" denoting an estimate.

In practice, a taper (e.g. Taylor, Hamming, etc) may be applied to $\bar{\mathbf{y}}(\ell)$ prior to (5) to reduce sidelobes in trade for a wider spectral mainlobe, and $\mathbf{A}$ "over-sampled" (i.e. $N \times M$ with $M \gg N$) to provide better visibility in frequency ω. We shall use the latter approach for super-resolution.

The straightforward STFT operation in (5) arises from modeling signals as a weighted superposition of sinusoids. A complete TF signal model can be expressed as

$$\begin{aligned}\bar{\mathbf{y}}(\ell) &= \sum_\omega \tilde{\mathbf{a}}(\omega)\,\tilde{s}_\text{f}(\ell,\omega) + \mathbf{b}(\ell) + \mathbf{v}(\ell) \\ &= \tilde{\mathbf{A}}\,\tilde{\mathbf{s}}_\text{f}(\ell) + \mathbf{b}(\ell) + \mathbf{v}(\ell),\end{aligned} \tag{6}$$

where $\mathbf{v}(\ell)$ is N samples of additive noise, the $N \times 1$ vector $\tilde{\mathbf{a}}(\omega) = [1\ e^{j\omega}\ e^{j2\omega} \cdots e^{j(N-1)\omega}]^T$ for arbitrary ω corresponds to complex amplitude $\tilde{s}_\text{f}(\ell,\omega)$, and $\mathbf{b}(\ell)$ is a catch-all for higher-order nonstationarity effects not perfectly represented by the collection of $\tilde{\mathbf{a}}(\omega)$ vectors. The top line of (6) implies a continuum in frequency, and thus the $\tilde{M} \times 1$ vector $\tilde{\mathbf{s}}_\text{f}(\ell)$ and $N \times \tilde{M}$ matrix $\tilde{\mathbf{A}}$ in the bottom line have $\tilde{M} \to \infty$.

Taken together, the frequency continuum and higher-order behaviors imply that any TF estimate will always possess some degree of error. That said, keeping N sufficiently small and $M \gg N$ means we can approximate (6) using the STFT approach in (5) via

$$\bar{\mathbf{y}}(\ell) \cong \mathbf{A}\,\mathbf{s}_\text{f}(\ell) + \mathbf{v}(\ell), \tag{7}$$

with the understanding that model error is unavoidable and therefore should be appropriately addressed when performing subsequent adaptive processing to achieve super-resolution.

Mathematically, (7) is a standard linear model and therefore appears identical to the idealized DF problem in which the discrete number of sources is generally assumed to be less than the number of antenna elements. Clearly the underlying model in (6) does not adhere to this discrete-source perspective, though we can still exploit the DF model-error framework from [15] to modify (7) as

$$\begin{aligned}\bar{\mathbf{y}}(\ell) &\cong [\mathbf{A}\,\mathbf{s}_\text{f}(\ell)] \odot \mathbf{z} + \mathbf{v}(\ell) \\ &= [\mathbf{A}\,\mathbf{s}_\text{f}(\ell)] + \mathbf{v}(\ell) + \mathbf{v}_\text{z}(\ell),\end{aligned} \tag{8}$$

with

$$\mathbf{v}_\text{z}(\ell) = (\mathbf{z} - \mathbf{1}_{N \times 1}) \odot [\mathbf{A}\,\mathbf{s}_\text{f}(\ell)] \tag{9}$$

incorporating model uncertainties incurred by discretization in frequency and any nonstationary effects. The nth element of $N \times 1$ vector $\mathbf{z}$ is (per [15])

$$z_n = [1 + \Delta_{\text{a},n}]e^{j\Delta_{\varphi,n}} \tag{10}$$

where the real-valued, independent random variables $\Delta_{\text{a},n}$ and $\Delta_{\varphi,n}$ respectively account for amplitude and phase errors.

III. RISR Adaptive Spectrogram

The RMMSE formulation [13] was originally derived to realize adaptive pulse compression for radar, and has since been experimentally demonstrated for applications spanning stretch processing [18], Doppler processing [19, 20], brain imaging [21] and more. By mapping the TF model into (8) and accounting for error-induced tolerances, an $N \times M$ bank of RMMSE filters $\mathbf{W}(\ell)$ is obtained by minimizing

$$J = E\{ \| \mathbf{s}_\text{f}(\ell) - \mathbf{W}^H(\ell)\,\bar{\mathbf{y}}(\ell) \|^2 \} \tag{11}$$

for $E\{\bullet\}$ denoting expectation.

Per the mathematically similar DF problem in [17], which also leverages the partial constraint form [16] to control the degree of super-resolution for robustness, (11) ultimately yields the mth adaptive spectrogram filter for the ith iteration as

$$\mathbf{w}_i(\ell,\omega_m) = \left[\frac{\left(\mathbf{P}_{m,m}(\ell) \right)^{1-\alpha}}{\left(\mathbf{a}^H(\omega_m)\,\mathbf{D}(\ell)\,\mathbf{a}(\omega_m) \right)^\alpha} \right] \mathbf{D}(\ell)\,\mathbf{a}(\omega_m) \tag{12}$$

for frequency ω_m and $0 \le \alpha \le 1$. A value of α near 0 yields the best frequency super-resolution, though smaller components may be suppressed, while α near 1 preserves small components with less super-resolution capability. Here $\mathbf{a}(\omega_m)$ is the mth column of $N \times M$ matrix $\mathbf{A}$ and

$$\mathbf{D}(\ell) = [\mathbf{R}(\ell) + \mathbf{R}_\text{z}(\ell) + \mathbf{R}_\text{v}]^{-1}, \tag{13}$$

for $\mathbf{R}_\text{v}$ the noise covariance, the structured signal component is

$$\mathbf{R}(\ell) = (\mathbf{A}\mathbf{P}(\ell)\,\mathbf{A}^H), \tag{14}$$

and the uncertainty component is

$$\mathbf{R}_\text{z}(\ell) = (\mathbf{A}\mathbf{P}(\ell)\,\mathbf{A}^H) \odot [\sigma_\text{z}^2\,\mathbf{I}_{N \times N}], \tag{15}$$

for σ_z^2 the variance of (9). The $M \times M$ matrix

$$\mathbf{P}(\ell) = E\{\mathbf{s}_\text{f}(\ell)\,\mathbf{s}_\text{f}^H(\ell)\} \tag{16}$$

is the time-localized spectral power density (diagonal by enforcing independence), with $\mathbf{P}_{m,m}(\ell)$ in (12) the mth diagonal element thereof.

In practice, $\mathbf{P}(\ell)$ from (16) is not known *a priori*, but is instead estimated for the ith iteration via

$$\hat{\mathbf{P}}_i(\ell) = \left[\frac{1}{2L+1} \sum_{\Delta\ell=-L}^{L} \hat{\mathbf{s}}_{\text{f},i-1}(\ell+\Delta\ell)\,\hat{\mathbf{s}}_{\text{f},i-1}^H(\ell+\Delta\ell) \right] \odot \mathbf{I}_{M \times M}, \tag{17}$$

where

$$\hat{\mathbf{s}}_{\text{f},i}(\ell) = \mathbf{W}_i^H(\ell)\,\bar{\mathbf{y}}(\ell) \tag{18}$$

comprises the complex amplitude estimates across the M frequencies for the ℓth snapshot at the ith iteration, and filter bank $\mathbf{W}_i(\ell)=[\mathbf{w}_i(\ell,\omega_1)\ \ \mathbf{w}_i(\ell,\omega_2)\ \ \cdots\ \ \mathbf{w}_i(\ell,\omega_M)]$. The process is initialized by setting $\mathbf{W}_{i=0}(\ell)=\mathbf{A}$ to obtain $\hat{\mathbf{s}}_{\mathrm{f},i=0}(\ell)$, with the RISR portion then sequentially applying (17), (12), and (18) for i = 1, 2, …, I_{iter} iterations. Setting $L = 0$ in (17) performs single-snapshot estimation for the finest time granularity, with higher L trading time granularity for a degree of noncoherent averaging over adjacent overlapping snapshots (i.e. smoothing).

IV. OPEN-AIR EXPERIMENTAL VALIDATION

In the companion paper [17], a self-calibrating version of RISR for DF (now "DF-RISR") was shown to provide enhanced spatial isolation. Here we sequentially combine DF-RISR with the adaptive RISR spectrogram (now "Freq-RISR") to separate the constituent signals in (2) prior to TF analysis. Practical assessment of Freq-RISR within this multi-signal context relies on the same open-air collection described in [17], where 8 wideband log-periodic antennas in a linear array configuration feed a Tektronix MSO68B oscilloscope (12.5 GHz sample rate digitally downconverted to 20 MHz), with λ/2 spacing at ~3.95 GHz (Fig. 1). The three emitters generate a 100% duty-cycle OFDM signal with 500 subcarriers (Tx1), a linear frequency modulated (LFM) chirp with 88% duty-cycle and 12.5 μs pulse duration (Tx2), and a random FM (RFM) waveform having a Gaussian power spectrum with 66% duty-cycle and 17.5 μs pulse duration (Tx3). All signals were centered at 3.82 GHz with a bandwidth of 10MHz. The transmit power of each was on the order of milliwatts, though Tx2 had ~10 dB higher gain.
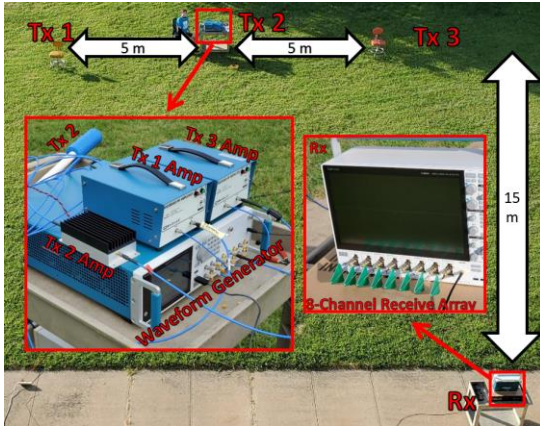

Fig. 1. Open-air experimental setup (see [17] for further details)

To demonstrate the prospective benefits of sequential spatial/TF adaptive processing, first a baseline case of nonadaptive TF processing with no spatial isolation (i.e. a single antenna element) is established. Assessment of spatial isolation and subsequent nonadaptive TF processing is then examined. Finally, the Freq-RISR adaptive spectrogram with and without spatial isolation via DF-RISR is considered, with these various processing arrangements illustrated in Fig. 2.

Fig. 3 first depicts the aggregated TF response of the receive-captured signal for a single antenna element (i.e. via Fig. 2a) with $N = 10$ and $M = 200$, which represents a baseline case without DF isolation or any form of adaptive enhancement. The time interval shown (45-65 μs) lies roughly in the center of the

collection interval shown in Fig. 3. We observe that the higher-power LFM clearly dominates, with the more random variation in frequency noticeable between ~47 and ~57 μs belonging to the RFM signal. The OFDM signal is not discernible.
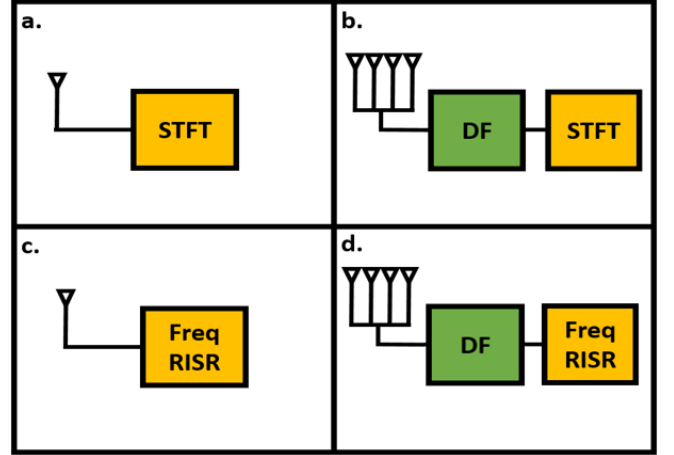

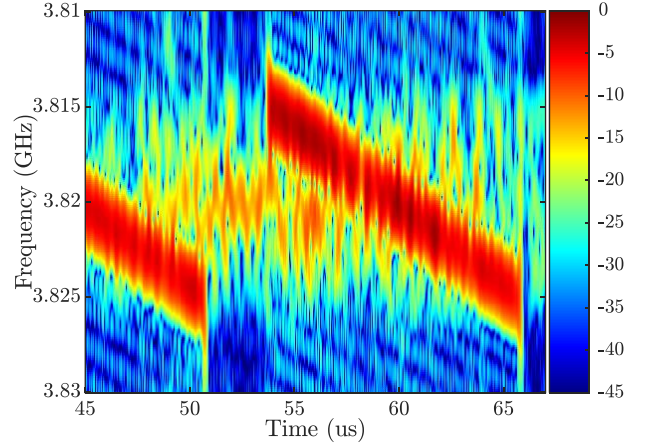**Fig. 2. Processing arrangements for open-air measurements**

Fig. 3. Aggregate spectrogram for a single antenna element (a.), showing the superimposed response of OFDM (Tx1), LFM (Tx2), and RFM (Tx3)

A. Nonadaptive TF Analysis of Spatially Isolated Signals

The comparison between DF-RISR and other methods (namely non-adaptive and MVDR) is discussed in [17]. Per Fig. 2b, we leverage the adaptive DF response that employs a sliding window of 15 time snapshots, which DF-RISR noncoherently averages in the same manner as (17). Fig. 4 illustrates the result obtained in [17] when DF-RISR is used, where the upper blue trace is the OFDM signal (Tx1), the middle red trace is the LFM signal (Tx2), and the lower yellow trace is the RFM signal (Tx3). The OFDM signal has the lowest receive power due to amplitude modulation, which also causes a slight variation in estimated angle over time.
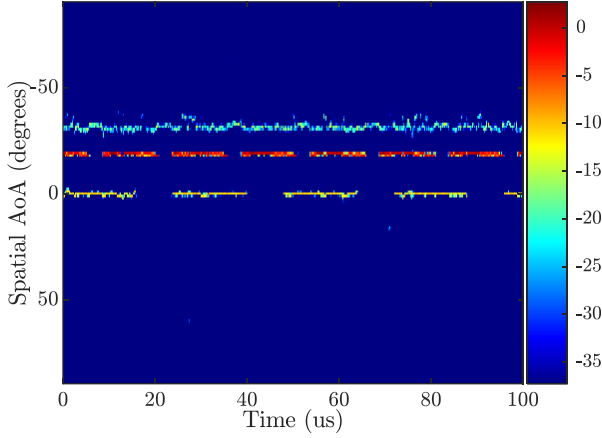
Fig. 4. Time-angle response from DF-RISR using 15 snapshots, with Tx1-OFDM (top), Tx2-LFM (middle), and Tx3-RFM (bottom)

Now consider performing standard spectrogram processing on the spatially isolated results from Fig. 4 obtained via DF-RISR [17]. To account for spatial estimation variability, which while notable for OFDM does occur to some degree for all three signals, a subtended angle is collected for each spatially isolated signal. These subtended angles comprise −40° to −28° for the OFDM signal (Tx1), −24° to −15° for LFM (Tx2), and −5° to +5° for RFM (Tx3). For each spatial interval, the maximum value is selected at each time sample in an attempt to preserve the dominant components resulting from adaptive DF processing (a mean operation could alternatively be used).

Figs. 5-7 show (peak-normalized) spectrogram responses for the DF-RISR isolated signals (for the case of Fig. 2b). The LFM response (Fig. 6) is still prominent, though visible contamination by other signals is now absent. The responses in Figs. 5 and 7 are even more significant, with the removal of LFM permitting the RFM and OFDM signals to be easily perceived. Note that while RFM has a single instantaneous frequency (it is FM), the OFDM response is flatter due to all 500 subcarriers being present throughout. Sharp pulse edges for LFM and RFM are also quite visible.
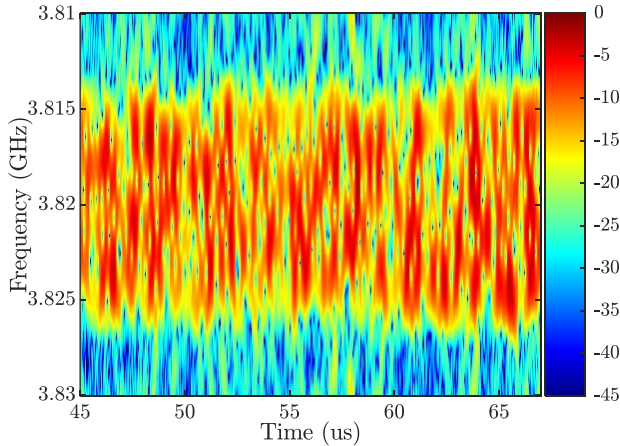

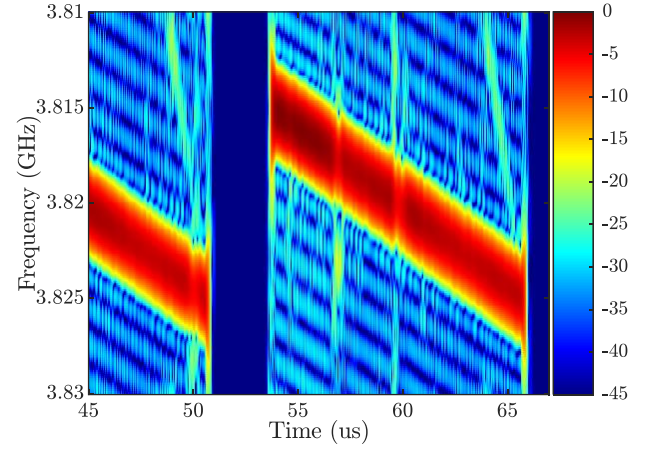**Fig. 5. Spectrogram of OFDM signal (Tx1) after DF-RISR spatial isolation**

Fig. 6. Spectrogram of LFM signal (Tx2) after DF-RISR spatial isolation
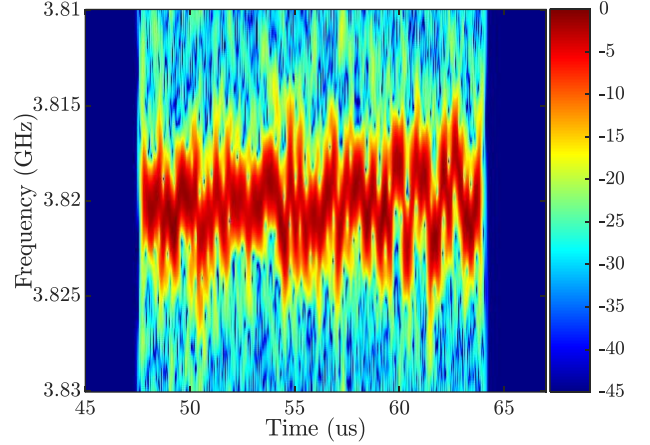

Fig. 7. Spectrogram of RFM signal (Tx3) after DF-RISR spatial isolation

By comparison, the non-adaptive and MVDR beamformers examined in [17] realize poorer spatial isolation, which in Figs. 8 and 9 translate into degraded TF results. Specifically, these standard spectrogram responses clearly exhibit cross-contamination for the non-adaptive beamformer, and even show degradation of the LFM spectrogram response following MVDR beamforming due to the use of low snapshot support (15, same as RISR). For instance, note the lack of clear pulse edges for LFM and RFM below compared to Figs. 6 and 7.
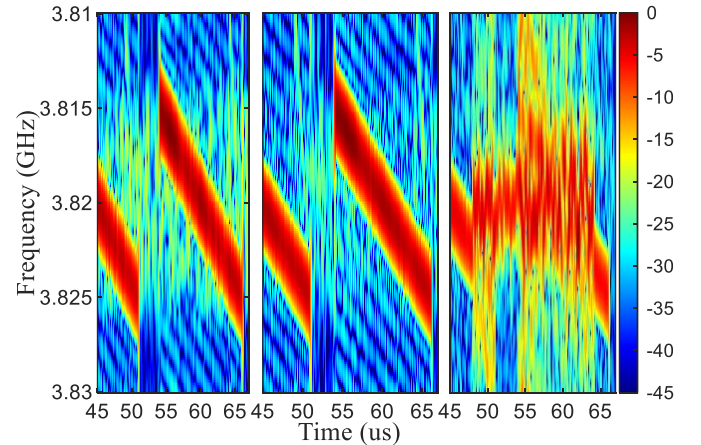

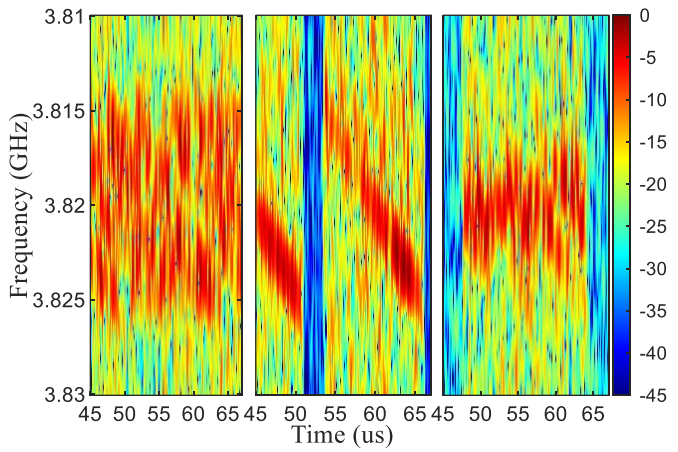**Fig. 8. Peak-normalized spectrograms from non-adaptive beamforming (left: OFDM, center: LFM, right: RFM)**

Fig. 9. Peak-normalized spectrograms from MVDR beamforming using 15 snapshots (left: OFDM, center: LFM, right: RFM)

B. Freq-RISR Analysis of Spatially Isolated Signals

Now consider the utility of adaptive TF analysis via Freq-RISR, which likewise uses $N = 10$ and $M = 200$, as well as 3 overlapping snapshots for smoothing (*i.e.* $L = 1$ per (17)), $\alpha = 0.6$, $\sigma_z^2 = 10^{-2}$, and 30 iterations. First the aggregated signal from Fig. 3 was processed with Freq-RISR (i.e. no spatial isolation via Fig. 2c), the result of which is shown in Fig. 10. What is immediately noticeable is that the time-localized frequency spread for the LFM signal is now far more compact, a consequence of super-resolution, with small perturbations in LFM frequency due to contamination from the other two signals (similarly visible in Fig. 3). It is difficult to discern which other parts correspond to RFM versus OFDM, despite the enhanced dynamic range being much greater than in Fig. 3.
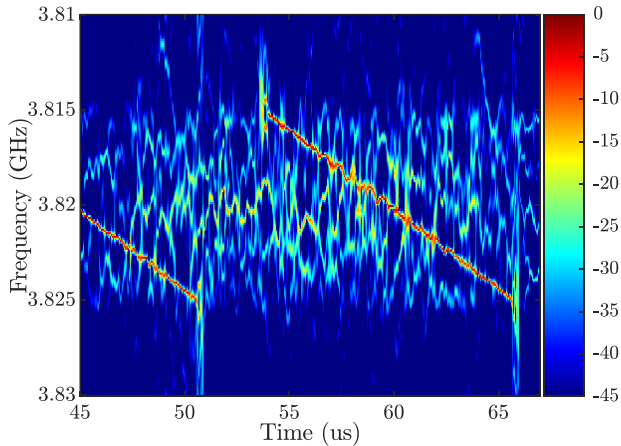

Fig. 10. Freq-RISR applied to aggregate signal from single antenna element

Figs. 11-13 then depict Freq-RISR adaptive TF responses following DF-RISR spatial isolation per Fig. 2d. For the OFDM signal (Fig. 11), the amplitude variation arising from 500 subcarriers realizes a TF response with variable peaks, though the 10 MHz bandwidth is still clearly delineated. It should be noted that the 10-sample window is far shorter than an OFDM symbol interval (here 50 μs, so ~1000 samples), which would require a factor of 200 in super-resolution (clearly not achieved) to isolate individual subcarriers in the 20 MHz band.

Consequently, the adaptive spectrogram response in Fig. 11 may not provide much further clarity compared to the standard response in Fig. 5 for this particular data instantiation.
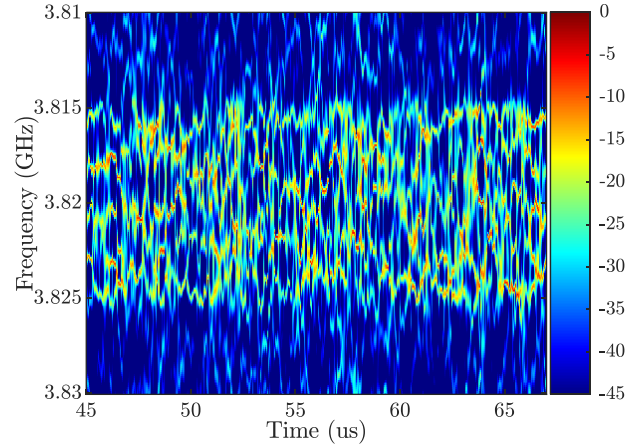

Fig. 11. Freq-RISR applied to DF-isolated OFDM signal (Tx1)

In contrast, the Freq-RISR response for the DF-RISR isolated RFM signal in Fig. 12 shows finer detail of the instantaneous frequency progression compared to the standard response of Fig. 7. That said, this meandering frequency path is broken up somewhat around the interval of 60-62 μs, which is the precise time when the higher-power LFM closely overlaps in frequency. It is possible that increasing the number of snapshots used for noncoherent averaging in DF and/or TF analysis could improve this result further, though other trade-offs may occur. The sharp pulse edges from Fig. 7 are also preserved.
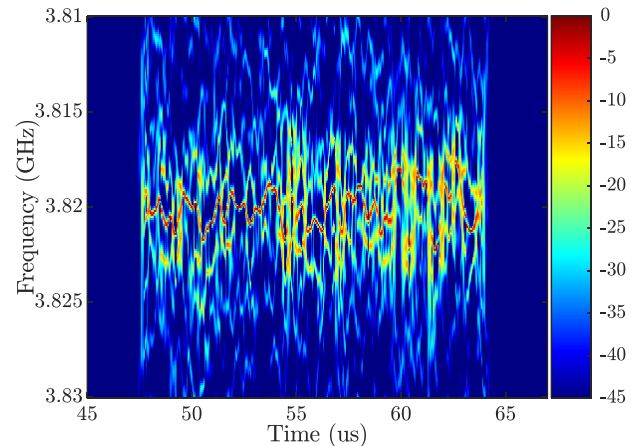

Fig. 12. Freq-RISR applied to DF-isolated RFM signal

Perhaps the most interesting Freq-RISR result occurs for the DF-RISR isolated LFM response (Fig. 13) since its predictable structure allows us to identify differences more easily. Now the chirping component is quite linear, with very little of the seemingly random deviations otherwise observed for the aggregate case in Fig. 10. Moreover, not only are the sharp pulse edges clearly delineated (like in Fig. 6), there are now broader spectral "flashes" at those points, which are indicative of the extended spectral content caused by the rapid rise/fall of each pulse. The meandering nature of RFM and lower SNR in

Fig. 12 made this effect harder to discern, though it should occur for any sharp pulse edges. Finally, from about 47-50 µs and again at roughly 63-66 µs in Fig. 13, there is another rapidly chirping component of much lower power, which appears to be a nonlinear distortion of the LFM. While these artifacts are visible in the standard response of Fig. 6, subtler features may now become available.
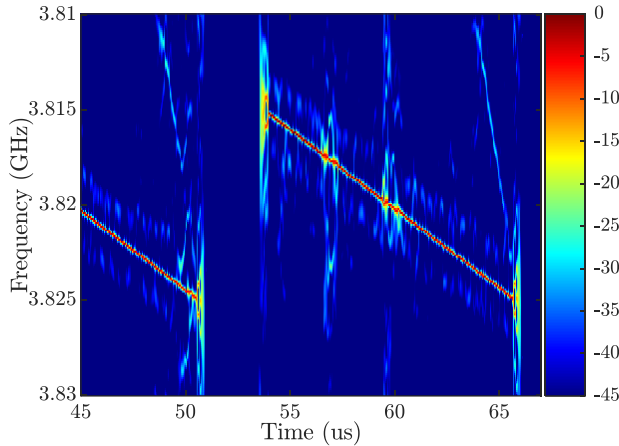

Fig. 13. Freq-RISR applied to DF-isolated LFM signal

The overall take away is that Freq-RISR, particularly when applied following effective spatial isolation such as via DF-RISR, is able to identify finer details of physical signals by achieving practical super-resolution and enhanced dynamic range. Consequently, the combination of these doubly adaptive responses with some manner of characterization/identification may prove rather useful for rapid and accurate discrimination of signals in increasingly complex and dynamic spectral environments in which DSA is required.

V. CONCLUSIONS

A form of RMMSE estimation has been used to formulate an adaptive approach to time/frequency (TF) analysis, achieving frequency super-resolution while preserving the nonstationary attributes afforded by fine time granularity. The resulting Freq-RISR method, when applied sequentially following the algorithmically similar DF-RISR method that adaptive achieves spatial isolation, is expected to provide improved signal characterization/identification in increasingly congested and dynamic RF environments, thereby supporting cognitive radar and related applications.

REFERENCES

[1] H. Griffiths, L. Cohen, S. Watts, E. Mokole, C. Baker, M. Wicks, S. Blunt, "Radar spectrum engineering and management: technical and regulatory issues," *Proc. IEEE*, vol. 103, no. 1, pp. 85-102, Jan. 2015.

[2] A. Martone, M. Amin, "A view on radar and communication systems coexistence and dual functionality in the era of spectrum sensing," *Digital Signal Processing*, June 2021.

[3] A.F. Martone, K.I. Ranney, K. Sherbondy, K.A. Gallagher, S.D. Blunt, "Spectrum allocation for noncooperative radar coexistence," *IEEE Trans. Aerospace & Electronic Systems*, vol. 54, no. 1, pp. 90-105, Feb. 2018.

[4] A. F. Martone, et al., "Closing the loop on cognitive radar for spectrum sharing," *IEEE Aerospace & Electronic Systems Mag.*, vol. 36, no. 9, pp. 44-55, Sept. 2021.

[5] B. Boashash, *Time-Frequency Signal Analysis and Processing*, 2016.

[6] E. Sejdić, I. Djurović, J. Jiang, "Time–frequency feature representation using energy concentration: An overview of recent advances", *Digital Signal Processing*, vol. 19, no. 1, pp. 153-183, Jan. 2009.

[7] F. Hlawatsch, G.F. Boudreaux-Bartels, "Linear and quadratic time-frequency signal representations," *IEEE Signal Processing Mag.*, vol. 9, no. 2, pp. 21-67, Apr. 1992

[8] B.P. Abbott, et al., "GW170817: Observation of gravitational waves from a binary neutron star inspiral", *Physical Review Letters*, vol. 119, Oct. 2017.

[9] S. Rahman, D.A. Robertson, "Radar micro-Doppler signatures of drones and birds at K-band and W-band," *Scientific Reports*, vol. 8, Nov. 2018.

[10] M. Lasseck, "Audio-based bird species identification with deep convolutional neural networks," *Conf. & Labs of Evaluation Forum*, Sept. 2018.

[11] S. Haykin, *Adaptive Filter Theory*, Prentice-Hall, 2002.

[12] R. Schmidt, "Multiple emitter location and signal parameter estimation," *IEEE Trans. Antennas & Propagation*, vol. 34, no. 3, pp. 276-280, Mar. 1986.

[13] S.D. Blunt, K. Gerlach, "Adaptive pulse compression via MMSE estimation," *IEEE Trans. Aerospace & Electronic Systems*, vol. 42, no. 2, pp. 572-584, July 2006.

[14] S. D. Blunt, T. Chan, K. Gerlach, "A new framework for direction-of-arrival estimation," *IEEE Sensor Array & Multichannel Signal Processing Workshop*, Darmstadt, Germany, July 2008.

[15] S.D. Blunt, T. Chan, K. Gerlach, "Robust DOA estimation: the reiterative superresolution (RISR) algorithm," *IEEE Trans. Aerospace and Electronic Systems*, vol. 47, no. 1, pp. 332-346, Jan. 2011.

[16] E. Hornberger, S.D. Blunt, T. Higgins, "Partially constrained adaptive beamforming for super-resolution at low SNR," *IEEE Intl. Workshop Computational Advances in Multi-Sensor Adaptive Processing*, Cancun, Mexico, Dec. 2015.

[17] C.C. Jones, Z.E. Gannon, D. DePardo, J.W. Owen, S.D. Blunt, C.T. Allen, B.H. Kirk, "Development & experimental assessment of robust direction finding and self-calibration" *IEEE Radar Conf.,* New York City, NY, Apr. 2022.

[18] L. Harnett, et al., "Optimal and adaptive mismatch filtering for stretch processing," *IEEE Radar Conf.*, Oklahoma City, OK, Apr. 2018.

[19] C.C. Jones, L.A. Harnett, C.A. Mohr, S.D. Blunt, C.T. Allen, "Structure-based adaptive radar processing for joint clutter cancellation and moving target estimation," *IEEE Intl. Radar Conf.*, Washington, DC, Apr. 2020.

[20] L.A. Harnett, B. Ravenscroft, S.D. Blunt, C.T. Allen, "Experimental evaluation of adaptive Doppler estimation for PRI-staggered radar," *IEEE Radar Conf.*, New York City, NY, Mar. 2022.

[21] M. Popescu, S.D. Blunt, T. Chan, "Magnetoencephalography source localization using the source affine image reconstruction (SAFFIRE) algorithm," *IEEE Trans. Biomedical Engineering*, vol. 57, no. 7, pp. 1652-1662, July 2010.